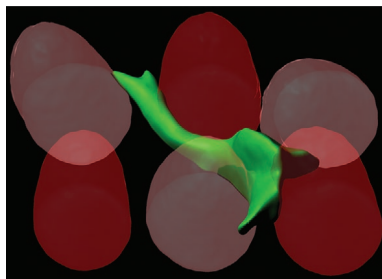


## FULL PAPERS

D. Devine, V. Vijayakumar, S. W. Wong,  
S. Lenzini, P. Newman,  
J.-W. Shin\* ..... 2000012

### **Hydrogel Micropost Arrays with Single Post Tunability to Study Cell Volume and Mechanotransduction**



A 3D printing approach has been developed to precisely control the placement and chemomechanical properties of individual hydrogel microposts that serve as discrete matrix signals to interface with cells. This approach serves as a platform to systematically investigate how elastic modulus and mechanical heterogeneity of microposts mediate cell volume and mechanotransduction.

# Hydrogel Micropost Arrays with Single Post Tunability to Study Cell Volume and Mechanotransduction

Daniel Devine, Vishwaarth Vijayakumar, Sing Wan Wong, Stephen Lenzini, Peter Newman, and Jae-Won Shin\*

The extracellular matrix varies considerably in mechanical properties at the microscale. It remains unclear how cells respond to these properties, in part, due to lack of tools to create precisely defined microenvironments in a discrete manner. Here, freeform stereolithography is leveraged to control the placement and elastic modulus of individual hydrogel microposts that serve as discrete matrix signals to interface with cells. Mesenchymal stromal cells (MSCs) located in the interstitial spaces between microposts above a base layer are analyzed. Cell volume is higher when MSCs interact with more microposts. MSCs show higher strain energy when they interact simultaneously with 4-kPa and 20-kPa microposts than with mechanically homogeneous micropost arrays. MSCs are sensitive to pharmacological inhibition of Rho-associated protein kinase in 4-kPa arrays, but resistant when presented together with 20-kPa arrays. Yes-associated protein (YAP) activity increases with higher cell volume and elastic modulus of microposts. Surprisingly, YAP activity becomes less variable with higher cell volume and decreases with higher average force and strain energy per post when MSCs interact with both 4-kPa and 20-kPa microposts simultaneously. Together, these results describe a material system for systematically investigating how the placement and intrinsic properties of discrete matrix signals impact cell volume and mechanotransduction.

## 1. Introduction

Mammalian cells exhibit striking diversity in size, which is tightly controlled to maintain organ size and functions.<sup>[1]</sup> However, cell size regulation remains poorly understood in the context of the extracellular matrix (ECM), which provides cells


with both physical signals and constraints. Mesenchymal stromal cells (MSCs) have served as an important model cell type to understand how physical properties of the ECM impact cell size and functions because they are highly mechanosensitive. On 2D substrates, matrix elasticity is known to mediate MSC volume by water flux.<sup>[2]</sup> Matrix elasticity also activates nuclear translocation of Yes-associated protein (YAP) in MSCs,<sup>[3]</sup> which is known to regulate cell volume.<sup>[4]</sup> In this context, the ability of cells to sense and respond to matrix elasticity requires force generation by actomyosin contractility,<sup>[5]</sup> which subsequently impacts various biological processes, including cell division,<sup>[6]</sup> differentiation,<sup>[7,8]</sup> migration,<sup>[9]</sup> and paracrine signaling.<sup>[10]</sup> In 3D substrates, degradable,<sup>[11]</sup> fast stress-relaxing<sup>[12]</sup> or microscale thin<sup>[13]</sup> hydrogels increase cell volume expansion, cell tension, and osteogenic differentiation of MSCs, while spatial confinement restricts these processes. Nuclear localization of YAP is enhanced in 3D hydrogels when MSCs are allowed to

spread or increase in cell volume as facilitated by stress relaxation, degradation or less crosslinking.<sup>[14–16]</sup> While these studies have revealed important insights into how the ECM mediates cell volume and mechanotransduction, the ECM varies considerably in biophysical properties at the microscale as revealed by mechanical force mapping of tissues.<sup>[17]</sup> This aspect of cell-matrix interactions is currently difficult to study using bulk engineered hydrogels, which lack control over microscale properties.

Combination of instrumentation and biomaterial design offers promising strategies to control the placement of matrix signals independently of their mechanics at microscale resolution. While electrospinning has been used to decouple polymer network architecture and mechanics by creating fibrous materials as a means to study mechanosensing of cells,<sup>[18]</sup> it is presently difficult to control where matrix fibers are placed. Microfabrication by stereolithography has the potential to precisely specify matrix mechanical properties at the microscale. So far, most studies have focused on 2D interaction of cells with micropatterned substrates as a means to study the effect of adhesion area,<sup>[19]</sup> geometry,<sup>[20–22]</sup> and surface topography<sup>[23]</sup> on MSC functions. Recently, micropatterning was used to study

D. Devine, V. Vijayakumar, Dr. S. W. Wong, S. Lenzini, Dr. P. Newman,<sup>[†]</sup> Prof. J.-W. Shin  
Department of Pharmacology and Regenerative Medicine  
University of Illinois at Chicago  
Chicago, IL, USA  
E-mail: shinjw@uic.edu

D. Devine, V. Vijayakumar, Dr. S. W. Wong, S. Lenzini, Dr. P. Newman, Prof. J.-W. Shin  
Department of Bioengineering  
University of Illinois at Chicago  
Chicago, IL, USA

 The ORCID identification number(s) for the author(s) of this article can be found under <https://doi.org/10.1002/adbi.202000012>.

<sup>[†]</sup>Present address: University of Sydney, Sydney, Australia

DOI: 10.1002/adbi.202000012

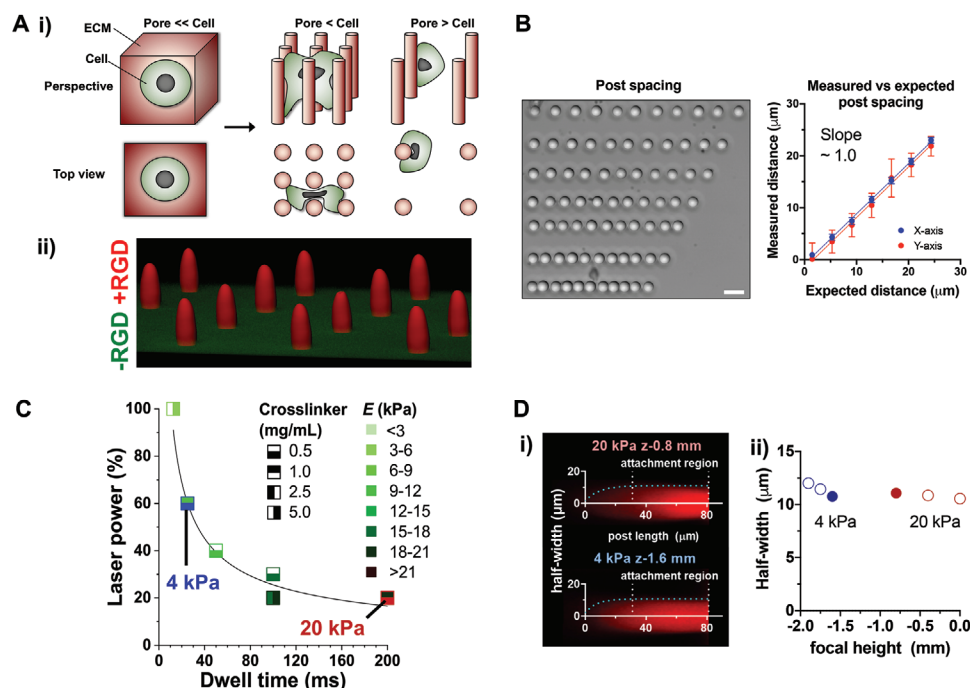


**Figure 1.** Controlling density and elastic modulus of hydrogel microposts. A) Strategy to control the presentation of matrix signals to cells. i) Schematic illustration of cells in matrices with different degrees of packing between matrix signals while preserving the intrinsic mechanical properties of materials. ii) A representative confocal image of a PEG-DA scaffold that enables cell adhesion only to posts (red). A 15  $\mu\text{m}$  PEG-DA base layer without cRGD peptide (green) was made before fabricating posts. Cysteine-containing cRGD (0.8 mM) was crosslinked throughout the posts during printing. B) Microscale control of spacing intervals during post printing (scale bar = 50  $\mu\text{m}$ ). Error bars in average versus expected spacing are reported as standard error of the mean (SEM) of the measured distance interval;  $n = 18$  per data point across 2 experiments. C) Controlling elastic modulus of posts by varying concentrations of crosslinker (lithium phenyl(2,4,6-trimethylbenzoyl)phosphinate), percent laser power and total dwell time. PEG-DA (25%) was used to fabricate all posts used in this study;  $n \geq 5$  posts per data point, each measured by AFM twice per post. Functional trend was fit to the two-parameter power series equation  $Y = a(1 + X)^b$ . D) Standardization of post curvature by changes in laser focal height. i)  $Z = -0.8$  mm and  $Z = -1.6$  mm focal heights were used to achieve regular post geometry between 20-kPa and 4-kPa posts, respectively. Cells attached predominantly to the linear region of the posts. Post curvatures were fitted to one-phase exponential association equation  $Y = Y_0 + (Y_{\text{max}} - Y_0)(1 - e^{-kx})$ . ii) Trends observed in 20-kPa and 4-kPa post half-widths based on fit equation. Post half-width corresponds to the  $Y_{\text{max}}$  of the exponential equation;  $n \geq 10$  posts per data point. Filled circles indicate half-width and focal height of microposts used in subsequent studies.

roles of 3D confinement geometry on single cell volume and downstream phenotypes of MSCs.<sup>[24]</sup> In another recent study, sidewalls of micropost substrates were selectively functionalized to allow adhesion of cells only to the interpost space, and subsequently show that MSCs become elongated as a function of stiffness anisotropy under spatial confinement.<sup>[25]</sup> However, it remains generally unclear how cells respond to different microscale matrix properties. Here, we describe a freeform stereolithography approach to fabricate hydrogel scaffolds consisting of microposts that serve as distinct matrix signals to interface with cells.

## 2. Results

### 2.1. Precisely Controlling the Placement and Mechanics of Individual Hydrogel Microposts

To independently control the placement and mechanics of the ECM at the microscale, we sought to fabricate arrays of hydrogel microposts that serve as distinct matrix signals to which cells can attach at various levels of post spacing (Figure 1Ai). To achieve this goal, we leveraged

stereolithography consisting of custom UV laser optics in a commercial three-axis printer that can deliver focused laser impulses to crosslink hydrogels at desired spatial locations<sup>[26]</sup> (Figure S1, Supporting Information). The posts consist of polyethylene glycol-diacrylate (PEG-DA) hydrogel covalently conjugated with the cyclic peptide consisting of Arg-Gly-Asp-D-Phe-Cys (cRGD) upon UV crosslinking,<sup>[27]</sup> while the base layer does not contain cRGD (Figure 1Aii). The system enables precise positioning of crosslinked posts with a spacing resolution of  $\approx 4$   $\mu\text{m}$  (Figure 1B). Decreased power but increased dwell time of the laser is essential to tune elastic or Young's modulus ( $E$ ) of posts within the same scaffold without changing crosslinker or PEG-DA concentrations as measured by atomic force microscopy (AFM) (Figure 1C), while maintaining a regular post diameter (Figure 1B). To standardize the geometry of the posts with  $\approx 22$   $\mu\text{m}$  diameter, the focal height of the laser was varied. In general, each post consists of a cylindrical part  $\approx 50$   $\mu\text{m}$  in length from the base layer, followed by an elliptical paraboloid shape  $\approx 30$   $\mu\text{m}$  in length (Figure 1Di). The laser focal height maintains the length of the cylindrical part but alters the width of the posts (Figure 1Dii), which also depends on  $E$ . Together, we optimized a freeform stereolithography system where the placement and elasticity of individual posts can be

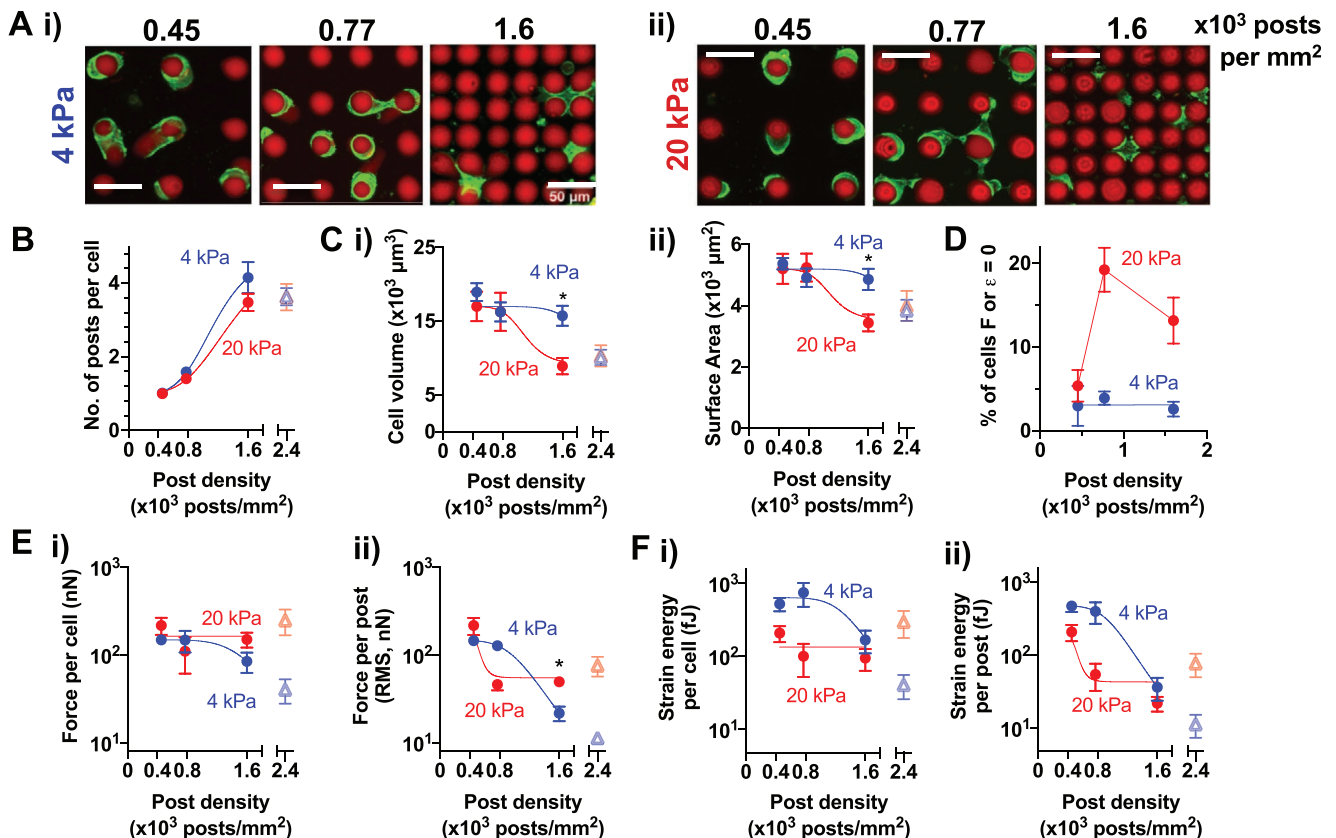


**Figure 2.** Micropost density and elastic modulus impact MSC volume, traction force, and strain energy. A) Representative images of live MSCs (green: plasma membrane stain) after 24 h of culture on i) 4-kPa and ii) 20-kPa post arrays (red). Scale bar = 50  $\mu\text{m}$ . B) The number of interacting microposts per cell. C) Quantification of cell i) volume and ii) surface area. D) Percent of cells that do not bend posts, where traction force or strain energy (see Methods) equals to zero. E) Traction force i) per cell and ii) per post. F) Strain energy i) per cell and ii) per post. All data points were plotted as a function of post density in 4-kPa or 20-kPa arrays. The data points showing monotonic changes as a function of post density were fitted to a dose-response curve,  $Y = \min + \frac{\max - \min}{1 + \left(\frac{\text{potency}}{\text{post density}}\right)^b}$ . Values for each graph in terms of (min, max, potency, b): (B) 4 kPa = (1, 5, 1175, 4.3), 20 kPa = (1, 5, 1404, 3.8); (C, i) 4 kPa = (9000, 17000, 1931, -8.9), 20 kPa = (9000, 17000, 1100, -7.1); (C, ii) 4 kPa = (3500, 5200, 1931, -8.6), 20 kPa = (3500, 5200, 1100, -7.0); (E, i) 4 kPa = (48, 147, 1464, -7.2); (E, ii) 4 kPa = (10, 148, 1057, -5.7), 20 kPa = (55, 213, 504, -10.5); (F, i) 4 kPa = (50, 639, 1385, -7.3); (F, ii) 4 kPa = (12, 476, 1007, -6.1), 20 kPa = (43, 208, 502, -10.0). \* $p < 0.05$ , two-way repeated measures ANOVA followed by Tukey's multiple comparisons testing. All error bars represent the SEM values across 3 different MSC donors;  $n \geq 70$  cells per donor. Open triangle symbols at post density  $2.4 \times 10^3$  posts  $\text{mm}^{-2}$  represent mean values from arrays with triangular post arrangement from  $n \geq 85$  cells (Figure S3, Supporting Information).

independently controlled within the same scaffold while standardizing the post geometry.

## 2.2. Micropost Density and Elastic Modulus Modulate Cell Volume, Traction Force, and Strain Energy

To characterize how micropost density and  $E$  impact cell volume and post deflection, human bone marrow-derived MSCs were seeded in micropost arrays with a physiologically relevant range of  $E \approx 4$  kPa or 20 kPa as used in previous mechanotransduction studies,<sup>[5]</sup> arranged into regular arrays of 0.45, 0.77 or  $1.6 \times 10^3$  posts  $\text{mm}^{-2}$  (Figure 2A). These densities were designed to introduce varying levels of spatial constraints to human MSCs, which show close to  $4000 \mu\text{m}^3$  in volume and  $\approx 1350 \mu\text{m}^2$  in surface area (roughly equivalent to

20  $\mu\text{m}$  in diameter) prior to spreading (Figure S2A, Supporting Information). Cells were seeded into scaffolds and cultured for 1 day before imaging to quantify cell volume and traction at the steady state. Cells that interact with the edge of scaffolds ( $\approx 20\%$ ) or undergo aggregation ( $\approx 10\%$ ) were excluded from the analysis (Figure S2B, Supporting Information). After excluding these cells, most cells primarily interact with the cylindrical region of the posts (Figure S2C, Supporting Information). To avoid any potential effect from the base layer, cells with z-position on posts between 11 and  $50 \mu\text{m}$  ( $\approx 70\%$  of the cells in the cylindrical region) were analyzed (Figure S2C,D, Supporting Information).

At higher micropost density, MSCs interact with more posts (Figure 2B) and are spatially confined (or “squeezed”) independent of micropost  $E$  (Figure S2E, Supporting Information), while the mean z-position of MSCs on posts is higher (Figure S2F, Supporting Information). Cell volume and surface

area of MSCs are more sensitive to micropost density with higher  $E$ : at  $1.6 \times 10^3$  posts  $\text{mm}^{-2}$ , cell volume is higher when  $E$  is 4 kPa than 20 kPa (Figure 2C). In contrast, cell volume remains the same with varied  $E$  on 2D hydrogels with the same polymer composition (Figure S2G, Supporting Information). As cells attach to matrix and generate forces, they pull on, bend, and bring matrix posts (or fibers) together to facilitate cell spreading.<sup>[18,21]</sup> The majority of MSCs deflect posts above the background level, which was used to estimate traction force ( $F$ ) and strain energy ( $\epsilon$ ) generated by each cell located at a given z-centroid height on posts (Figure S2H, Supporting Information; see Methods).<sup>[28]</sup> The percentage of cells that do not bend posts ( $F$  or  $\epsilon = 0$ ) is increased with higher post density for 20-kPa microposts (Figure 2D). Subsequent analyses were done for the population of cells that bend posts ( $F$  or  $\epsilon > 0$ ). Traction force and strain energy per cell remain constant with increased micropost density in 20-kPa micropost arrays, while they are decreased in 4-kPa post arrays—effectively, this leads to higher average force per post (calculated as root mean square or RMS force; see Methods) when  $E$  is higher at the highest micropost density, while average strain energy per post remains the same (Figure 2E,F). To increase micropost density further while keeping the same post interval ( $\approx 6 \mu\text{m}$ ), MSCs were placed in microposts arranged into triangular grids with  $2.4 \times 10^{-3}$  posts  $\mu\text{m}^{-2}$  (Figure S3A, Supporting Information). At this density, the mean number of posts per cell remains unchanged, but cell volume, average force, and strain energy per post are further decreased in 4-kPa microposts (Figure S3B, Supporting Information). Thus, both  $E$  and micropost density are important determinants of cell volume, traction force, and strain energy.

### 2.3. Scaling of Cell Volume, Traction Force, and Strain Energy with the Number of Microposts

Under higher spatial confinement ( $1.6 \times 10^3$  posts  $\text{mm}^{-2}$ ), MSCs interact with different numbers of microposts with the mean number  $\approx 3.8$  posts per cell when posts are 4-kPa and 3.0 per cell when posts are 20-kPa (Figure 3A). In general, regardless of  $E$ , cell volume is larger when MSCs interact with more posts, exhibiting power law behavior with scaling exponent ( $\alpha$ )  $\approx 1.7$  (Figure 3B). The traction force per cell also scales with the number of interacting microposts, while it remains generally higher for MSCs in 20-kPa arrays than in 4-kPa arrays (Figure 3Ci). Interestingly, average force per post scales only weakly with the number of posts for MSCs in 20-kPa micropost arrays ( $\alpha \approx 0.6$ ), while it scales well with the number of posts for MSCs in 4-kPa posts ( $\alpha \approx 1.3$ ) (Figure 3Cii). While the strain energy per cell is higher in 20-kPa arrays than in 4-kPa arrays when MSCs interact with only two posts, it becomes equivalent and scales with the number of posts when MSCs interact with more than two posts (Figure 3Di). As with average force per post, average strain energy per 20-kPa post scales weakly with the number of posts ( $\alpha \approx 0.7$ ), while it scales well with the number of posts for MSCs in 4-kPa arrays ( $\alpha \approx 1.3$ ) (Figure 3Dii). Consistent with previous studies,<sup>[21,22]</sup> a higher traction force per cell in 20-kPa arrays is associated with increased focal adhesion formation in live MSCs (Figure S4,

Supporting Information). Thus, micropost  $E$  determines scaling between average force or strain energy per post and the number of interacting posts per cell.

### 2.4. MSCs Enhance Strain Energy When They Interact Simultaneously with 4-kPa and 20-kPa Microposts

To study how heterogeneity in discrete matrix mechanical signals impacts cell volume and traction forces under spatial confinement, MSCs were seeded in printed scaffolds of alternating 4-kPa and 20-kPa micropost arrays (“mixed”  $E$  micropost arrays) at  $1.6 \times 10^3$  posts  $\text{mm}^{-2}$ —this arrangement was chosen to maximize the chance that MSCs interact simultaneously with 4-kPa and 20-kPa posts (Figure 4A). As expected, MSCs interact with 4-kPa and 20-kPa microposts equally regardless of the number of interacting posts (Figure 4B). As with mechanically homogeneous micropost arrays, MSCs interact with different numbers of microposts within mixed  $E$  arrays with the mean number  $\approx 3.0$  posts per cell (Figure 4C). Cell volume also scales with the number of interacting microposts, with higher  $\alpha \approx 2.1$ , suggesting that simultaneous interaction of 4-kPa and 20-kPa posts drives a higher cell volume increase than interaction with 4-kPa or 20-kPa posts alone (Figure 4D). Traction force per cell scales with the number of posts in mixed  $E$  arrays in a similar manner as in 20-kPa arrays (Figure 4Ei). However, unlike 20-kPa arrays, average force per post scales well with the number of posts ( $\alpha \approx 1.3$ ) in mixed  $E$  arrays (Figure 4Eii). Interestingly, both strain energy per cell and average strain energy per post in mixed  $E$  arrays are higher than in 20-kPa arrays and scale well with the number of posts (Figure 4F). Together, the scaling of cell volume with the number of interacting microposts accompanies a greater generation of strain energy in mechanically heterogeneous micropost arrays.

### 2.5. Elastic Modulus and Mechanical Heterogeneity Mediate the Sensitivity of MSCs to ROCK Inhibition

Myosin-II plays an important role in driving contractility to generate traction forces in both 2D and 3D environments.<sup>[8,11,18]</sup> To understand how myosin impacts cell volume and traction forces in different mechanical environments under spatial confinement, MSCs in scaffolds were treated with a pharmacological inhibitor of Rho-associated kinase (ROCK), Y27632. Y27632 reduces average force and strain energy per post (Figure 5A, i, ii), as well as cell volume and the number of interacting posts per cell for MSCs in 4-kPa micropost arrays (Figure 5Aiii, iv). Rac1 and Cdc42 are known to stabilize newly formed protrusions.<sup>[29]</sup> Inhibition of Cdc42 by ML141, but not Rac1 by NSC23766 also reduces average force and strain energy per post, and cell volume in 4-kPa arrays; however, the number of interacting posts remains unchanged (Figure S5A, Supporting Information). In contrast, MSCs in 20-kPa microposts are resistant to perturbation by Y27632 (Figure 5A), as well as perturbation by ML141 and NSC23766 (Figure S5B, Supporting Information). F-actin expression remains unchanged by Y27632 (Figure S5C, Supporting Information), consistent with previous studies showing reduced



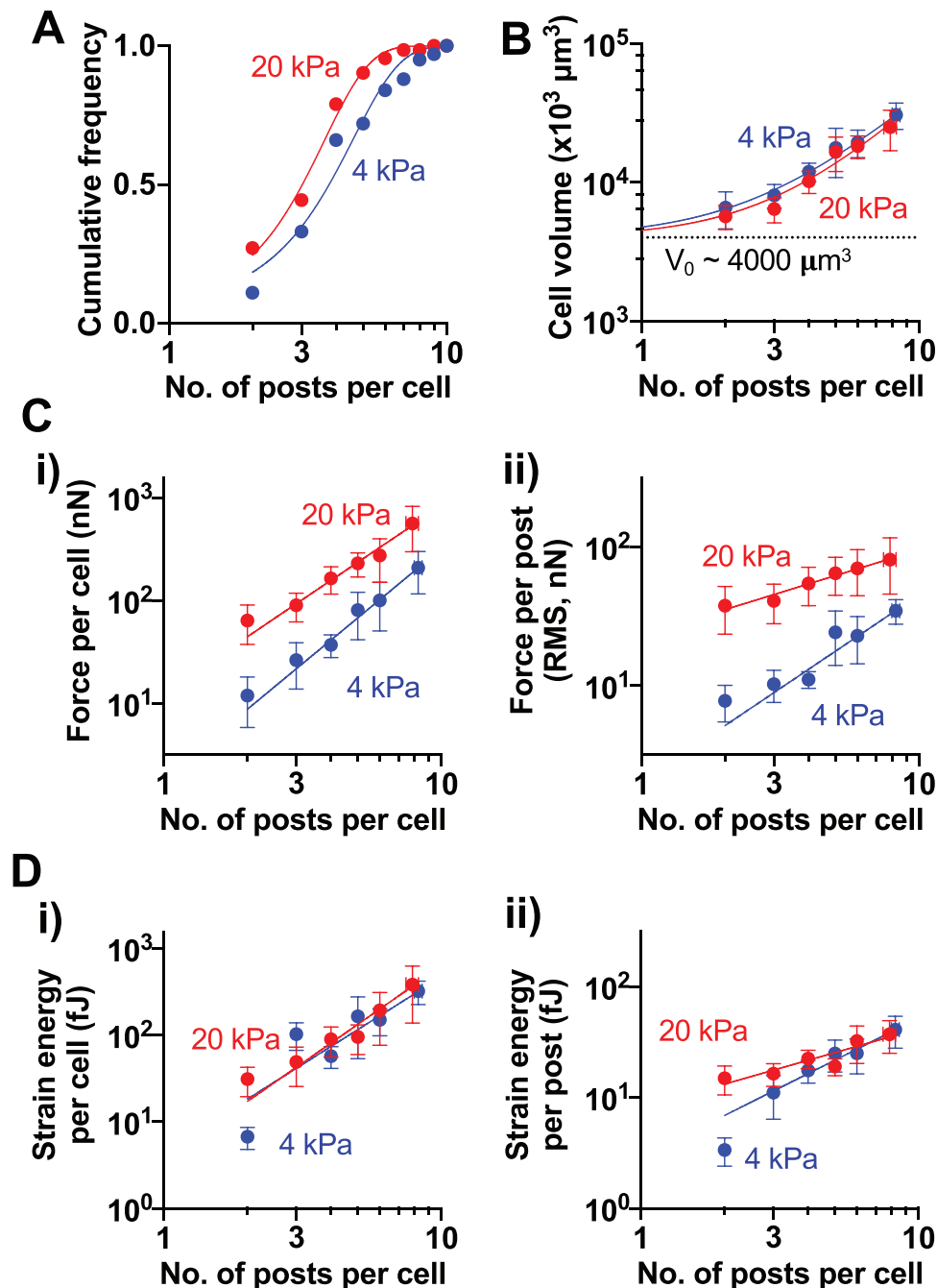


**Figure 3.** Scaling of cell volume, traction force, and strain energy with the number of interacting microposts in mechanically homogeneous arrays. A) Cumulative frequency distribution of the number of posts ( $n_{\text{post}}$ ) contacted by MSCs cultured for 24 h in 4 kPa or 20 kPa arrays. The  $n_{\text{post}}$  Mean  $\pm$  SD: 4 kPa =  $3.78 \pm 1.97$ ; 20 kPa =  $3.02 \pm 1.48$ . B) Scaling of cell volume with  $n_{\text{post}}$ . C) Scaling of traction force i) per cell and ii) per post with  $n_{\text{post}}$ . D) Scaling of strain energy i) per cell and ii) per post with  $n_{\text{post}}$ . For (B)-(D), All data points were fitted to a power law equation,  $Y = A_0 + A \cdot n_{\text{post}}^\alpha$ . Values for each graph in terms of ( $A_0$ ,  $A$ ,  $\alpha$ ): (B) 4 kPa = (4000, 752.6, 1.7), 20 kPa = (4000, 510.4, 1.7); (C, i) 4 kPa = (0, 2.2, 2.2), 20 kPa = (0, 13.1, 1.8); (C, ii) 4 kPa = (0, 2.0, 1.3), 20 kPa = (0, 23.8, 0.6); (D, i) 4 kPa = (0, 4.5, 2.0), 20 kPa = (0, 3.7, 2.2); (D, ii) 4 kPa = (0, 3.5, 1.3), 20 kPa = (0, 6.8, 0.7). All error bars represent 95% confidence intervals.  $n \geq 94$  cells pooled from 2 donors for each  $E$  array, grouped based on  $n_{\text{post}}$ .

actin turnover and F-actin stabilization with myosin inhibition.<sup>[30]</sup> Inhibition of actin polymerization by Latrunculin A reduces average force and average strain energy on both 4-kPa and 20-kPa microposts, while it reduces cell volume and the number of interacting posts for MSCs in 4-kPa but not in

20-kPa arrays (Figure S5B, Supporting Information). To analyze the impact of ROCK on the ability of MSCs to deflect 4-kPa and 20-kPa microposts in mixed  $E$  arrays, average force and strain energy per post were calculated separately for each post  $E$ . Average force and strain energy on 4-kPa posts become

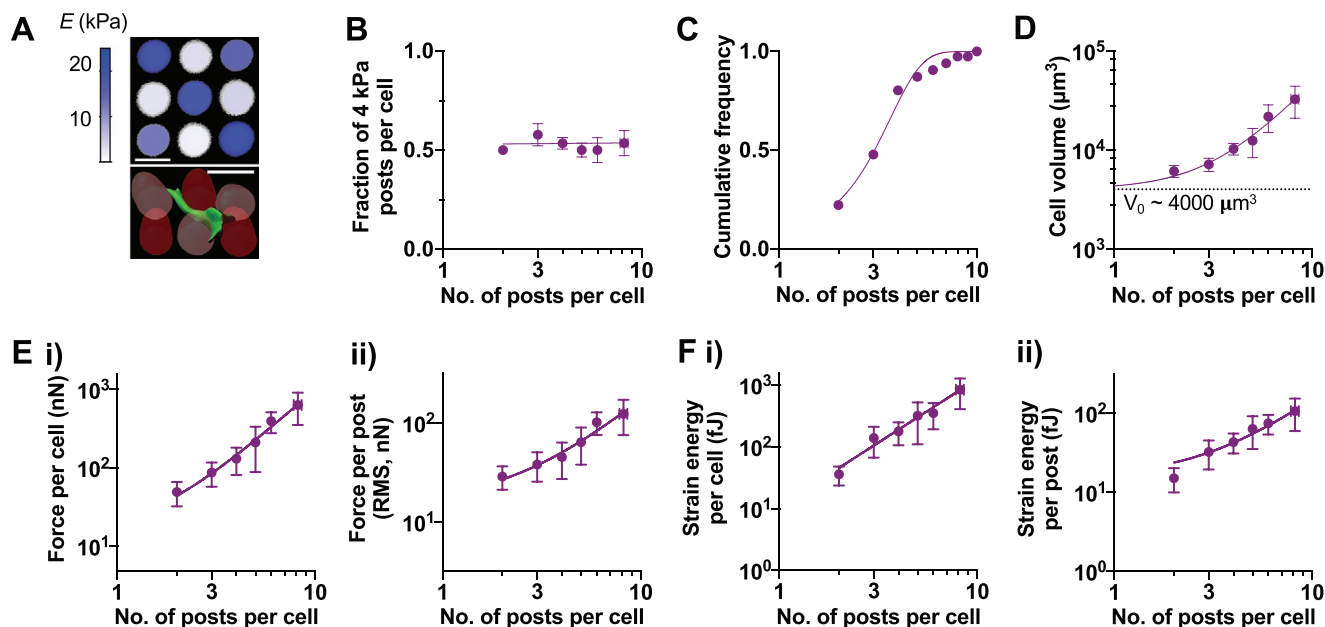


**Figure 4.** Scaling of cell volume, traction force, and strain energy with the number of interacting microposts in mechanically heterogeneous arrays. A) Representative images. (Top) Confocal stack maximum intensity projection of representative mixed post arrays, colorized according to elastic modulus as measured by AFM. Scale bar = 25  $\mu\text{m}$ . (Bottom) 3D reconstruction of a live MSC in mixed post arrays. Dark red: 20-kPa post, light red: 4-kPa post, green: human MSC labeled with plasma membrane stain. B) Fraction of 4-kPa posts contacted by each cell as a function of the number of interacting posts per cell ( $n_{\text{post}}$ ). The data were fitted to  $Y = 0.52$ . C) Cumulative frequency distribution of  $n_{\text{post}}$  in mixed arrays. Mean  $\pm$  SD =  $3.04 \pm 1.48$ . D) Scaling of cell volume with  $n_{\text{post}}$ . E) Scaling of traction force i) per cell and ii) per post with  $n_{\text{post}}$ . F) Scaling of strain energy i) per cell and ii) per post with  $n_{\text{post}}$ . For (D)–(F), all data points were fitted to a power law equation,  $Y = A_0 + A \times n_{\text{post}}^\alpha$ . Values for each graph in terms of ( $A_0$ ,  $A$ ,  $\alpha$ ): (D) = (4000, 328.7, 2.1); (E, i) = (0, 8.5, 2.1); (E, ii) = (0, 9.5, 1.3); (F, i) = (0, 10.9, 2.1); (F, ii) = (0, 7.7, 1.3). All error bars represent 95% confidence intervals;  $n = 117$  cells pooled from 2 donors, grouped based on  $n_{\text{post}}$ .

resistant to Y27632 perturbation when MSCs interact simultaneously with 20-kPa posts in mixed  $E$  arrays (Figure 5B). Thus, the sensitivity of MSCs to ROCK inhibition depends on  $E$  and mechanical heterogeneity of the micropost array environment.

## 2.6. Elastic Modulus and Mechanical Heterogeneity Impact YAP Activity in Hydrogel Micropost Arrays

Given the role of YAP in mechanotransduction,<sup>[3]</sup> YAP activity in live MSCs was evaluated as a function of  $E$  and mechanical heterogeneity in hydrogel micropost arrays. Prior to cell seeding in arrays, MSCs were transfected with a reporter construct that expresses red fluorescence protein (RFP) in response to YAP binding, which is stabilized only in the presence of trimethoprim (TMP) due to a destabilization domain (DD) as described<sup>[31]</sup> (Figure 6Ai; Figure S6, Supporting Information). YAP activity is higher for MSCs in 20-kPa arrays than in 4-kPa arrays—however, despite greater strain energy (Figures 3 and 4), YAP activity in mixed  $E$  arrays remains lower than in 20 kPa arrays (Figure 6Aii). YAP activity scales with cell volume in 4-kPa or 20-kPa arrays with  $\alpha \approx 0.5$  (Figure 6Bi). In contrast, YAP activity scales with cell volume in mixed arrays with a lower  $\alpha \approx 0.2$  (Figure 6Bii). While YAP activity remains higher with increased  $E$ , it does not scale with average force per post for both 4-kPa and 20-kPa arrays (Figure 6Ci). Surprisingly, YAP activity decreases with average force per post in mixed  $E$  arrays (Figure 6Cii). The same results can also be seen with average strain energy

per post (Figure 6D). Thus, YAP activity is less coupled from changes in cell volume and even decreases with higher average force and strain energy per post in mixed  $E$  posts.

## 3. Discussion

The freeform stereolithography approach enables precise control of microscale mechanical properties by curing one micropost at a time to fabricate a hydrogel scaffold. Our approach is distinct from previous studies in that cells can be present in closely spaced posts and receive distinct mechanical signals simultaneously. Fabricating arrays of posts that serve as distinct matrix signal units has enabled us to derive a quantitative relationship between cell-matrix interactions and cellular phenotypes in terms of discrete microposts.

Our approach controls the coordinates and mechanics of individual microposts within a hydrogel scaffold, created from the same base material and composition by adapting a relatively low-cost ( $\sim$ \\$2000) commercial printer to deliver UV laser impulses to specific locations at single-cell resolution. In this approach, increased dwell time but decreased power of the UV laser leads to increased elastic modulus of posts while post geometry remains regular. Thus, sustained delivery of UV light, in addition to UV light dose, appears to be important to achieve higher hydrogel crosslinking within a focal region. This insight will be useful to develop a generalizable model to predict a wide range of microscale hydrogel mechanics and geometry as a

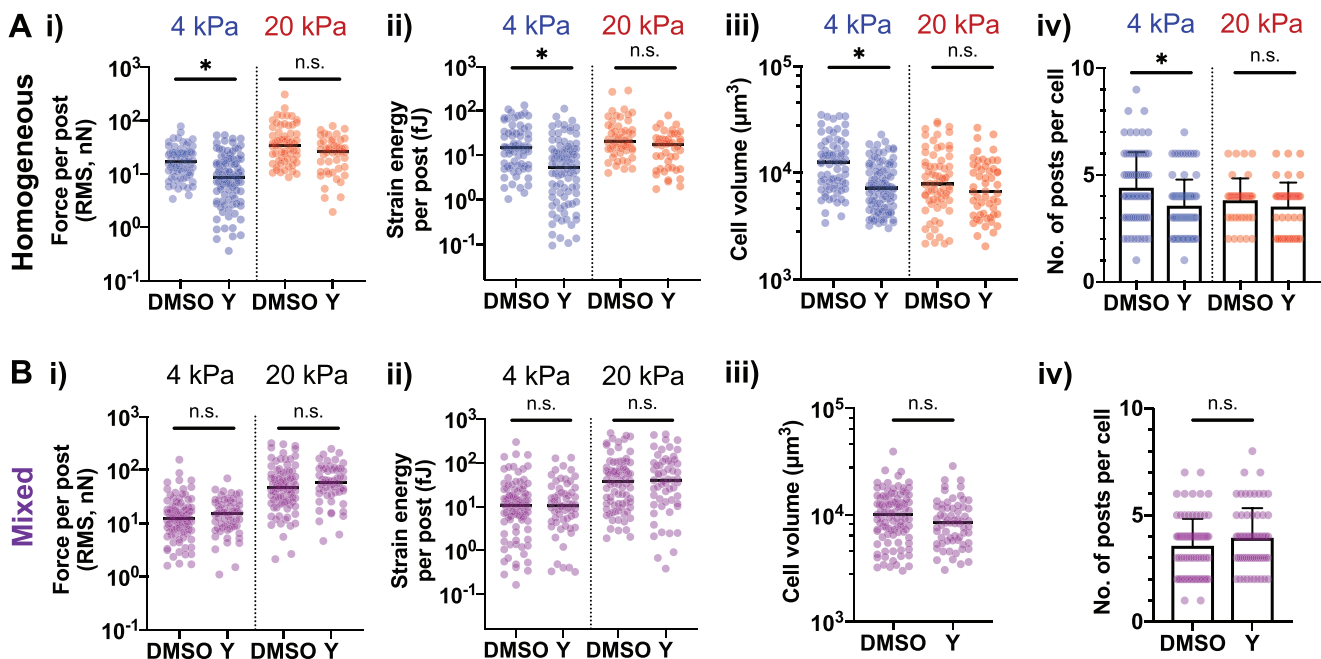


**Figure 5.** MSCs respond differentially to ROCK inhibition as a function of micropost elastic modulus and mechanical heterogeneity. After seeding MSCs in micropost arrays for 24 hours, they were treated with DMSO or the ROCK inhibitor Y27632 (“Y”, 10  $\mu$ M) for 24 hours prior to analysis. Effects of ROCK inhibition on MSCs in A) mechanically homogeneous arrays and B) mechanically heterogeneous (mixed) arrays. For (A) and (B), i) Average force per post, ii) Average strain energy per post, iii) cell volume, and iv) number of interacting posts per cell. \* $p < 0.05$ , two-tailed Mann-Whitney test. For (i)–(iii), median values are shown, and error bars in (iv) represent SD;  $n \geq 40$  cells for each array type (4-kPa, 20-kPa, mixed) treated with DMSO versus Y27632, pooled from 3 independent experiments, 1 donor.

function of a base material and laser parameters. Developing the model will be important to advance the utility of freeform stereolithography in fabricating scaffolds to study cell functions.

Our results show that elastic modulus and mechanical heterogeneity differentially affect cell volume, traction forces, sensitivity to ROCK inhibition, and YAP activity under spatial confinement. Recent studies highlight the complexity of mechanotransduction in 3D microenvironments. For covalent, purely elastic 3D hydrogels, degradability and less crosslinking (low  $E$ ) enable increased cell volume, traction forces, and nuclear YAP localization in a myosin-dependent manner, leading to increased osteogenic differentiation of MSCs.<sup>[11,15,32]</sup> For physically crosslinked, viscoelastic 3D hydrogels, fast stress relaxation increases cell volume, traction forces, and osteogenic differentiation of MSCs, but YAP does not play a role in these processes.<sup>[12,14,33]</sup> Studies with 3D microwells in covalent hydrogels show that there exists an optimal space per cell where actin polymerization, focal adhesion, and nuclear YAP localization are enhanced regardless of hydrogel stiffness.<sup>[24]</sup> Our hydrogel micropost system offers different ways to decouple the parameters related to cell volume regulation and mechanosensing. For instance, MSCs increase cell volume by interacting with more posts, while keeping mean traction force and average strain energy less variable in 20-kPa posts (Figure 3). In addition, arrays with alternating 4-kPa and 20-kPa posts can be used to decouple cell volume and traction forces from YAP activity (Figure 6). Thus, the results from the mixed  $E$  arrays generally mirror some of the previous observations with viscoelastic 3D gels; whether mechanical heterogeneity at a cellular

level results in faster stress relaxation at a tissue level remains to be investigated. However, one important difference is the resistance of MSCs to ROCK inhibition with mechanical heterogeneity (Figure 5). Interestingly, a recent study presents a myosin-independent mechanism of force generation to drive cell spreading by actin polymerization.<sup>[34]</sup> Future studies will investigate roles of different actin polymerization regulators in sensing of mechanically heterogeneous environments. In addition, it will be important to study whether there exist a unique transcription factor that can be activated in response to mechanical heterogeneity. Our approach will also allow systematic investigations into the effect of micropost arrangement and topology in mechanically heterogeneous environments on cell volume and mechanotransduction. This study opens new avenues of investigation into how distinct matrix biophysical properties work together at the microscale to influence different aspects of mechanobiology, such as durotaxis and mechanically-directed lineage specification of stem cells.

## 4. Experimental Section

**Glass Surface Modification:** To covalently bond crosslinked hydrogel to the print surface, acrylate groups were attached to glass coverslips by silanization as described.<sup>[33]</sup> Briefly, a solution of 3% v/v 3-(trimethoxysilyl)propyl acrylate (A1597, TCI) and 5% v/v glacial acetic acid (#A38, Fisher Scientific) was prepared in methanol. 10 mm  $\times$  10 mm No. 1 coverslips (#260375-1, Ted Pella) were incubated in the reaction solution for 45 minutes and thoroughly washed with methanol. The newly silanized coverslips were rinsed with ethanol and dried.



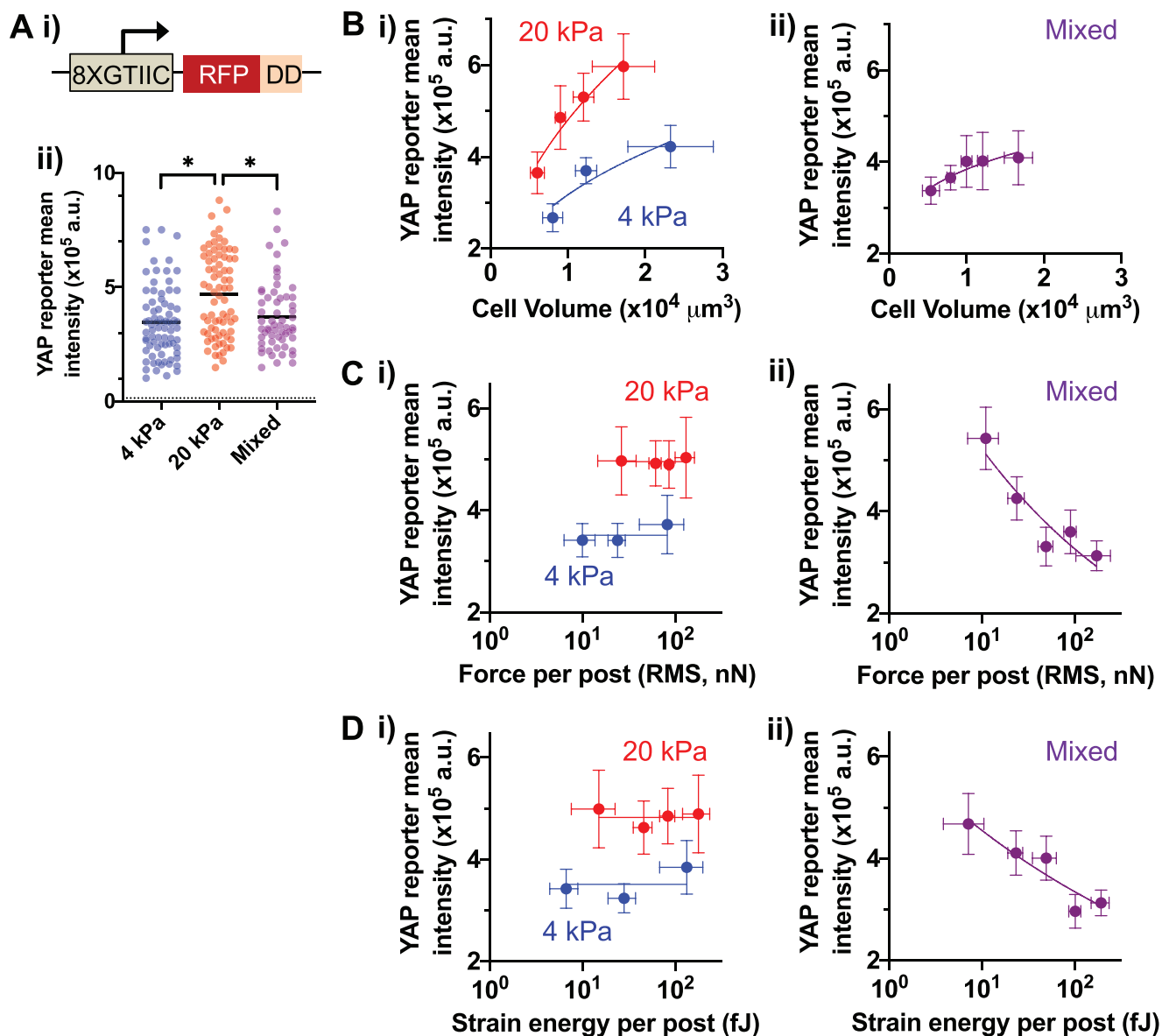


**Figure 6.** Elastic modulus and mechanical heterogeneity of micropost arrays mediate YAP activity. A) Quantification of YAP activity in live MSCs. i) A YAP-responsive promoter (8XGTIIC) drives the expression of RFP fused with a DD. RFP is stably expressed only in the presence of TMP that stabilizes the DD. ii) YAP reporter (RFP) mean intensity of MSCs in different micropost arrays. A dotted line indicates the background RFP mean intensity value in the absence of TMP.  $*p < 0.05$ , Kruskal-Wallis test, followed by Dunn's multiple comparisons test. Black lines represent the median for each group. B) YAP activity as a function of cell volume in i) mechanically homogeneous arrays and ii) mixed arrays. C) YAP activity as a function of average force per post in i) mechanically homogeneous arrays and ii) mixed arrays. For (B), (C, ii) and (D, ii), data points were fitted to a power law equation  $Y = A_0 + A.X^\alpha$ . Values for each group in terms of ( $A_0$ ,  $A$ ,  $\alpha$ ): (B, i) 4 kPa = ( $10^5$ , 2135, 0.5), 20 kPa = ( $10^5$ , 2379, 0.5); (B, ii) = ( $10^5$ , 30414, 0.2); (C, ii) = ( $10^5$ ,  $2.6 \times 10^6$ , -0.3); (D, ii) = ( $10^5$ ,  $1.1 \times 10^6$ , -0.2). For (C, i) and (D, i), data points were fitted to a linear equation,  $Y = A_0$  with slope = 0.  $A_0$  for each group: (C, i) 4 kPa =  $3.5 \times 10^5$ , 20 kPa =  $5.0 \times 10^5$ ; (D, i) 4 kPa =  $3.5 \times 10^5$ ,  $4.8 \times 10^5$ . All error bars in (B)-(D) represent 95% confidence intervals;  $n \geq 60$  cells for each array type (4-kPa, 20-kPa, and mixed), pooled from 3 independent experiments, 1 donor.

**Hydrogel Preparation:** To create hydrogel solutions as previously described,<sup>[27]</sup> 10 mM sodium L-ascorbate (#A7631, Sigma-Aldrich), 4 mM tris(2-carboxyethyl)phosphine (#C4706, Sigma-Aldrich), 1X PBS (#P5493, Sigma-Aldrich) and 0.8 mM cRGD cell adhesion peptide (#303458, NovoPro) were prepared in sterile-filtered diH<sub>2</sub>O. PEG-DA  $M_n$  700 (#455008, Sigma-Aldrich) and lithium phenyl(2,4,6-trimethylbenzoyl) phosphinate (#L0290, TCI Chemicals) were added in varying concentrations to achieve desired range in Young's modulus upon UV

exposure. Hydrogel mixtures were briefly degassed by sonication prior to use. To restrict cell attachment to only post scaffolds, cRGD was omitted from the hydrogel base layer solution.

**Hardware for Freeform Stereolithography:** A three-axis Hyrel Engine SR printer (Hyrel 3D) was modified with a modular print head consisting of 500 mW 405 nm laser (M-33A405-500-G), aspheric collimating lens (#A240TM, Thor Labs), iris diaphragm (#SM1D12D, Thor Labs) and aspheric focusing lens (#AL1225H, Thor Labs), by adapting previously

described hardware designs.<sup>[26]</sup> The print head circuit utilized an Arduino Uno R3 microcontroller and metal oxide semiconductor field-effect transistor (MOSFET: FQP30N06L) to modulate laser power at high frequency. A command to power the laser prompted the printer to send a 12V digital signal to the print head circuit at a frequency and peak width that varied according to the percentage power specified. The signal first passed through circuitry that utilized two resistors to step the signal down to 4.8V before being read by the Arduino. The Arduino measured the percentage of time the signal was on over a 20  $\mu$ s period, and generated a square wave output signal at constant frequency by pulse width modulation; the pulse width determined the proportion of on/off switching (duty cycle) of the MOSFET that controlled power cycling of the laser. The Arduino also enabled specification of the frequency and scaling of signal output, which were set to 244 Hz and 10%, respectively. Thus, a command to increase % power caused a higher frequency signal with broader peaks to be sent to the Arduino, which ultimately increased the proportion of time the diode emitted light at a constant frequency—thereby increasing the continuity and intensity (wattage) of UV emission. The laser diode circuit was connected to constant current regulator (B01N7CG71M) to maintain a steady 4.8V signal to the laser. A photodiode power sensor (#S120VC, Thorlabs) and a power meter console (#PM100A, Thorlabs) were used to calibrate laser power output.

**Fabrication of Scaffolds by Freeform Stereolithography:** To fabricate scaffolds with arrays of microscale posts, silanized no. 1 (0.15 mm) coverslips were placed into a print chamber made of two 75 mm  $\times$  25 mm  $\times$  1 mm glass slides spin coated with polydimethylsiloxane (SYLGARD 184 silicone elastomer kit) and separated by spacers positioned on opposite ends of the slides. The chamber height was determined by spacer thickness: 0.17 mm during preparation of the scaffold base layer, and 0.25 mm during scaffold post printing and 2D PEG gel fabrication. For scaffolds, each coverslip was first coated with a PEG-DA hydrogel solution. The top chamber slide was placed over the solution, followed by UV lamp exposure for 90 seconds (#40322, Dymax)—leading to a 15  $\mu$ m base layer to which cells cannot attach. The base layer was gently washed, and another PEG-DA solution with cRGD was added to the chamber; the cysteine contains a thiol group which bonds to the acrylate in PEG-DA during UV exposure. To crosslink posts directly onto the base layer, laser impulses were focused at discrete points along the coverslip using the printer. To fabricate 2D PEG gels, hydrogel solution containing cRGD was placed in the print chamber and crosslinked by UV lamp exposure for 60 seconds. Fabricated scaffolds and 2D gels were gently washed for  $\approx$ 1–3 days by rocking overnight in hank's balanced salt solution (HBSS: #14175079, Thermo Fisher Scientific) containing 100 U mL<sup>-1</sup> penicillin/streptomycin (P/S: #15140122, Thermo Fisher Scientific) prior to cell seeding.

**Shape Characterization of Printed Scaffolds:** To determine the diameter and spacing of printed microposts, images were taken under brightfield microscope at 20X magnification (Nikon Eclipse Ts2R), and distances between posts were measured with Fiji software package by drawing a line between the boundaries of adjacent posts. To measure height and curvature, microposts were printed with Rhodamine B Isothiocyanate-containing hydrogel and washed in HBSS for 2 hours. Confocal stack images were acquired at 20X magnification using a Zeiss 710 Laser Scanning Microscope as described earlier. Images of posts along the axial plane were produced from the stack, and points along the post border converted to a coordinate system that defined X as the length dimension of each post and Y as the width dimension. Each post was aligned symmetrically along the X-axis, and all Y coordinates were made positive. Coordinates were then fitted to the one-phase association equation  $Y = Y_0 + (Y_{\max} - Y_0)(1 - e^{-kx})$  to characterize curvature and post diameter ( $Y_{\max} = \frac{1}{2}$  post width) (Figure 1D).

**MSC Isolation and Expansion:** Human MSCs were isolated by plastic adherence ("passage 0") of mononuclear cells from primary human bone marrow aspirates (Lonza) followed by culture for 10–14 days to achieve 80–90% confluence in the growth media consisting of nucleoside-free MEM alpha (#12561, Thermo Fisher Scientific), 20% fetal bovine serum (FBS: #S11550, Atlanta Biologicals), 100 U mL<sup>-1</sup>

P/S and 1% GlutaMAX (#35050061, Thermo Fisher Scientific). MSCs were subsequently expanded up to three passages (within 30 days of total culture time) at 80% confluency ( $\approx$ 7-day intervals) before cryopreservation in 10% dimethyl sulfoxide (DMSO: #D8418, Sigma-Aldrich), 50% FBS and 40% growth media and stored in liquid nitrogen. No difference was observed among tested donors in terms of the rate of proliferation. Passage numbers between "2" and "4" or up to 38 total culture days from initial plastic adherence were used for experiments. All cells tested negative for mycoplasma.

**Cell Seeding in Printed Scaffolds:** For imaging experiments, MSCs were trypsinized, resuspended in growth media, and passed twice through a 40  $\mu$ m cell strainer (#352340, Corning) to remove cell aggregates. Cells were counted, and  $2.5 \times 10^4$  cells were suspended in 2 mL of imaging media and added to the prints in a 24 well ultra-low attachment plate (#3473, Corning). Seeded prints were gently rocked for 5 hours at room temperature in the culture media consisting of 10% FBS, FluoroBRITE DMEM, 100 U mL<sup>-1</sup> P/S and 1% GlutaMAX, and transferred to 37 °C overnight.

**Image Analysis to Evaluate Cell Volume, Traction Force, and Strain Energy:** Cells on prints were stained in the culture media with 1:1000 NucSpot Live 650 nuclear stain (#40082, Biotium) and 1:1000 CellMask green plasma membrane stain (#C37608, Thermo Fisher Scientific) at 37 °C for 60 minutes. Cellular stains were prepared per manufacturer's protocols. Stained prints were washed, gently placed onto 40  $\times$  22 coverslips and covered in FBS-free imaging media throughout image acquisition. Images were acquired at 10X magnification using a Zeiss LSM 710 confocal microscope by capturing individual slices of the lateral (xy) plane at 1  $\mu$ m increments along the axial (z) plane. These image stacks were imported into Imaris for 3D reconstruction (Bitplane) and volume/surface area measurements. Incomplete renderings of cell surfaces, aggregations and cells attached to irregular posts or on the border of scaffolds were not included in analysis (Figure S2B, Supporting Information). Cell surface renderings were flattened into a 2D image and converted to binary colorization to trace cell boundaries using the MATLAB (Natick, MA) Image Processing Toolbox which was used to quantify post bending. Each cell was given a unique ID to further analyze individual cells in terms of post contact and bending. The 3D reconstructed post images were sliced into xy images at 1  $\mu$ m thickness along the z direction and binarized. For posts each cell contacted, centroids of the posts were calculated at the base of each post ( $z = 0$ ) and at a height equivalent to that of the centroid of the cell in the z-axis in the respective post z-stack images (Figure S2H, Supporting Information). Vectors were calculated between the two centroids representing the uncorrected post deflection. For each grid, an average background noise vector was calculated for each post type: 4 and 20 kPa, where no cells were attached to the post. The average magnitude of the background noise vector was then subtracted from the magnitude of the deflection of each measured post to calculate the corrected magnitude of the post deflection ( $\delta$ ). An elastic, Hookean traction force was calculated for each post using the equation below as described:<sup>[21,36]</sup>

$$F = \frac{3\pi ED^4}{64L^3} \delta = k\delta \quad (1)$$

where  $E$  is the elastic modulus (4 or 20 kPa),  $D$  is the diameter of the post (22  $\mu$ m) and  $L$  is the distance from the base of the post to the centroid of the cell in the z-direction.

A total traction force per cell was calculated by adding the magnitude of the individual traction forces of each post. An average magnitude of force per post generated by each cell was calculated as RMS force ( $F_{RMS}$ ) as described:<sup>[37]</sup>

$$F_{RMS} = \sqrt{\frac{\sum_{i=1}^n F_i^2}{n}} \quad (2)$$

where  $F_i$  is the traction force on each post and  $n$  is the total number of posts touched by a cell.

For each post, the strain energy applied to the post was calculated to estimate cellular contractility as described:<sup>[36]</sup>

$$E = \frac{1}{2} \frac{3\pi ED^4}{64L^3} \delta^2 = \frac{1}{2} k \delta^2 \quad (3)$$

The total strain energy per cell was calculated by the scalar addition of the individual strain energies of each post. The average strain energy per post was calculated by dividing the total strain energy per cell by the total number of posts touched by a cell.

**Drug Treatment:** For inhibitor studies, MSCs were seeded in micropost arrays for 24 hours. MSCs were then treated with either DMSO (1:10000 dilution) or Y27632 (10  $\mu$ M) for 24 hours at 37 °C prior to imaging as above. For other inhibitors, MSCs were treated with either DMSO, NSC23766 (10  $\mu$ M), ML141 (10  $\mu$ M) or latrunculin A (0.25  $\mu$ M) for 4 hours prior to imaging. All drugs were purchased from Cayman Chemical.

**Quantification of Fluorescently Labelled Proteins in Live Cells:** To quantify YAP activity, focal adhesion, and F-actin in live MSCs seeded in hydrogel microposts, MSCs were transfected with pTRE-8XGTIIIC-DsRED-DD ("YAP RFP reporter"), Paxillin-RFP or mTagRFP-T-LifeAct-7 ("LifeAct-RFP"), respectively. pTRE-8XGTIIIC-DsRED-DD was a gift from Joan Massague (Addgene plasmid #115798). Paxillin-RFP was a gift from Andrei Karginov (UIC). mTagRFP-T-LifeAct-7 was a gift from M. Davidson (Addgene plasmid #54586). Each plasmid (2  $\mu$ g) and 500000 cells were mixed in 100  $\mu$ l of nucleofection buffer from the human MSC nucleofector kit (VPE-1001, Lonza) and electroporated using a high-viability program in Amaxa (Lonza). Transfected cells were then cultured on plastic overnight. After seeding transfected cells in hydrogel microposts and cultured for an additional day, cells were then stained with CellMask Green and NucSpot Live 650, followed by confocal imaging analysis as described above. To quantify the expression of YAP RFP reporter, a mean projection image was created from each confocal stack and mean intensity of RFP per cell was analyzed by ImageJ (NIH). To quantify paxillin-RFP and LifeAct-RFP signals, cells that express fluorescence signals were imaged, followed by analysis using Imaris. Thresholding values were kept constant across all samples. Gaussian filtering was used to smooth the CellMask Green signal, and the boundary of the reconstructed voxel was defined as the cell surface. A paxillin cluster was defined as any distinct paxillin-RFP signal below the cell surface with voxel volume > 0.001  $\mu$ m<sup>3</sup>. Analysis was done on every single paxillin-RFP cluster for each cell. For F-actin, the total volume of LifeAct-RFP per cell was measured.

**Atomic Force Microscopy:** Printed scaffolds were immersed in a drop of HBSS. A silicon nitride cantilever with an 18° pyramid tip (MLCT, Bruker) was used for nanoindentation. The spring constant of the cantilever was determined from thermal fluctuations before each experiment. Indentation was performed under contact mode with force-distance 500 nm at 1  $\mu$ m s<sup>-1</sup> velocity, until trigger voltage (0.5 V) is reached, followed by retraction. *E* was then calculated by fitting a force-indentation curve to the Hertzian model with Poisson's ratio at 0.5. About 10–15 posts were measured for each scaffold, and two independent experiments were performed.

**Statistical Analysis:** Statistical hypothesis tests were performed in GraphPad Prism. For data that do not show normal distributions based on Anderson-Darling test, Mann-Whitney test was used to compare two groups, and Kruskal-Wallis test followed by Dunn's multiple comparisons test was used to compare more than two groups. For data that show normal distributions but variable standard deviations, Welch's *t*-test was used to compare two groups. For two-factor analysis, such as volume as a function of post density and elastic modulus, repeated measures two-way ANOVA with Geisser-Greenhouse correction was used, followed by Tukey's multiple comparisons testing. A *p*-value less than 0.05 established statistical significance.

## Supporting Information

Supporting Information is available from the Wiley Online Library or from the author.

## Acknowledgements

D.D., V.V., and S.W.W. contributed equally to this work. The authors gratefully acknowledge Dr. Peter Toth and the Core Imaging Facility at UIC for technical help on confocal imaging, and Dylan Lynch (UIC) and Karl Gifford (Hyrel) for technical help on the printer hardware. This work was supported by National Institutes of Health Grant R01-HL141255 (J.-W.S.) and R00-HL125884 (J.-W.S.).

## Conflict of Interest

The authors declare no conflict of interest.

## Keywords

cell volume, extracellular matrix, hydrogels, mechanobiology, microposts

Received: January 16, 2020

Revised: September 28, 2020

Published online:

- [1] A. C. Lloyd, *Cell* **2013**, *154*, 1194.
- [2] M. Guo, A. F. Pegoraro, A. Mao, E. H. Zhou, P. R. Arany, Y. Han, D. T. Burnette, M. H. Jensen, K. E. Kasza, J. R. Moore, F. C. Mackintosh, J. J. Fredberg, D. J. Mooney, J. Lippincott-Schwartz, D. A. Weitz, *Proc. Natl. Acad. Sci. USA* **2017**, *114*, E8618.
- [3] a) S. Dupont, L. Morsut, M. Aragona, E. Enzo, S. Giullitti, M. Cordenonsi, F. Zanconato, J. Le Digabel, M. Forcato, S. Bicciato, N. Elvassore, S. Piccolo, *Nature* **2011**, *474*, 179; b) Z. Meng, Y. Qiu, K. C. Lin, A. Kumar, J. K. Placone, C. Fang, K. C. Wang, S. Lu, M. Pan, A. W. Hong, T. Moroishi, M. Luo, S. W. Plouffe, Y. Diao, Z. Ye, H. W. Park, X. Wang, F. X. Yu, S. Chien, C. Y. Wang, B. Ren, A. J. Engler, K. L. Guan, *Nature* **2018**, *560*, 655.
- [4] N. A. Perez-Gonzalez, N. D. Rochman, K. Yao, J. Tao, M. T. Le, S. Flanary, L. Sablich, B. Toler, E. Crensil, F. Takaesu, B. Lambrus, J. Huang, V. Fu, P. Chengappa, T. M. Jones, A. J. Holland, S. An, D. Wirtz, R. J. Petrie, K. L. Guan, S. X. Sun, *J. Cell Biol.* **2019**, *218*, 3472.
- [5] D. E. Discher, P. Janmey, Y. L. Wang, *Science* **2005**, *310*, 1139.
- [6] J. W. Shin, A. Buxboim, K. R. Spinler, J. Swift, D. A. Christian, C. A. Hunter, C. Leon, C. Gachet, P. C. Dingal, I. L. Ivanovska, F. Rehfeldt, J. A. Chasis, D. E. Discher, *Cell Stem Cell* **2014**, *14*, 81.
- [7] J. Swift, I. L. Ivanovska, A. Buxboim, T. Harada, P. C. Dingal, J. Pinter, J. D. Pajerowski, K. R. Spinler, J. W. Shin, M. Tewari, F. Rehfeldt, D. W. Speicher, D. E. Discher, *Science* **2013**, *341*, 1240104.
- [8] A. J. Engler, S. Sen, H. L. Sweeney, D. E. Discher, *Cell* **2006**, *126*, 677.
- [9] M. Raab, J. Swift, P. C. Dingal, P. Shah, J. W. Shin, D. E. Discher, *J. Cell Biol.* **2012**, *199*, 669.
- [10] S. W. Wong, S. Lenzini, M. H. Cooper, D. J. Mooney, J. W. Shin, *Sci. Adv.* **2020**, *6*, eaaw0158.
- [11] S. Khetan, M. Guvendiren, W. R. Legant, D. M. Cohen, C. S. Chen, J. A. Burdick, *Nat. Mater.* **2013**, *12*, 458.
- [12] H. P. Lee, R. Stowers, O. Chaudhuri, *Nat. Commun.* **2019**, *10*, 529.
- [13] S. W. Wong, S. Lenzini, R. Bargi, Z. Feng, C. Macaraniag, J. C. Lee, Z. Peng, J. W. Shin, *Adv. Sci.* **2020**, <https://doi.org/10.1002/advs.202001066>.
- [14] O. Chaudhuri, L. Gu, D. Klumpers, M. Darnell, S. A. Bencherif, J. C. Weaver, N. Huebsch, H. P. Lee, E. Lippens, G. N. Duda, D. J. Mooney, *Nat. Mater.* **2016**, *15*, 326.
- [15] S. R. Caliri, S. L. Vega, M. Kwon, E. M. Soulas, J. A. Burdick, *Biomaterials* **2016**, *103*, 314.

- [16] M. Bao, J. Xie, N. Katoele, X. Hu, B. Wang, A. Piruska, W. T. S. Huck, *ACS Appl. Mater. Interfaces* **2019**, *11*, 1754.
- [17] a) I. L. Ivanovska, J. Swift, K. Spinler, D. Dingal, S. Cho, D. E. Discher, *Mol. Biol. Cell* **2017**, *28*, 2010; b) F. Liu, J. D. Mih, B. S. Shea, A. T. Kho, A. S. Sharif, A. M. Tager, D. J. Tschumperlin, *J. Cell Biol.* **2010**, *190*, 693.
- [18] B. M. Baker, B. Trappmann, W. Y. Wang, M. S. Sakar, I. L. Kim, V. B. Shenoy, J. A. Burdick, C. S. Chen, *Nat. Mater.* **2015**, *14*, 1262.
- [19] R. McBeath, D. M. Pirone, C. M. Nelson, K. Bhadriraju, C. S. Chen, *Dev. Cell* **2004**, *6*, 483.
- [20] K. A. Kilian, B. Bugarija, B. T. Lahn, M. Mrksich, *Proc. Natl. Acad. Sci. USA* **2010**, *107*, 4872.
- [21] J. Fu, Y. K. Wang, M. T. Yang, R. A. Desai, X. Yu, Z. Liu, C. S. Chen, *Nat. Methods* **2010**, *7*, 733.
- [22] S. J. Han, K. S. Bielawski, L. H. Ting, M. L. Rodriguez, N. J. Sniadecki, *Biophys. J.* **2012**, *103*, 640.
- [23] M. J. Dalby, N. Gadegaard, R. Tare, A. Andar, M. O. Riehl, P. Herzyk, C. D. Wilkinson, R. O. Oreffo, *Nat. Mater.* **2007**, *6*, 997.
- [24] M. Bao, J. Xie, A. Piruska, W. T. S. Huck, *Nat. Commun.* **2017**, *8*, 1962.
- [25] Y. Alapan, M. Younesi, O. Akkus, U. A. Gurkan, *Adv. Healthcare Mater.* **2016**, *5*, 1884.
- [26] a) Q. A. Tran, V. Ajeti, B. T. Freeman, P. J. Campagnola, B. M. Ogle, *Stem Cells Int.* **2018**, *2018*, 4809673; b) B. D. Fairbanks, M. P. Schwartz, C. N. Bowman, K. S. Anseth, *Biomaterials* **2009**, *30*, 6702; c) V. Chan, J. H. Jeong, P. Bajaj, M. Collens, T. Saif, H. Kong, R. Bashir, *Lab Chip* **2012**, *12*, 88.
- [27] J. Zhu, C. Tang, K. Kottke-Marchant, R. E. Marchant, *Bioconjugate Chem.* **2009**, *20*, 333.
- [28] N. J. Sniadecki, C. S. Chen, *Methods Cell Biol.* **2007**, *83*, 313.
- [29] M. Machacek, L. Hodgson, C. Welch, H. Elliott, O. Pertz, P. Nalbant, A. Abell, G. L. Johnson, K. M. Hahn, G. Danuser, *Nature* **2009**, *461*, 99.
- [30] a) J. W. Shin, J. Swift, K. R. Spinler, D. E. Discher, *Proc. Natl. Acad. Sci. USA* **2011**, *108*, 11458; b) C. A. Wilson, M. A. Tsuchida, G. M. Allen, E. L. Barnhart, K. T. Applegate, P. T. Yam, L. Ji, K. Keren, G. Danuser, J. A. Theriot, *Nature* **2010**, *465*, 373.
- [31] E. E. Er, M. Valiente, K. Ganesh, Y. Zou, S. Agrawal, J. Hu, B. Griscorn, M. Rosenblum, A. Boire, E. Brogi, F. G. Giancotti, M. Schachner, S. Malladi, J. Massague, *Nat. Cell Biol.* **2018**, *20*, 966.
- [32] L. G. Major, A. W. Holle, J. L. Young, M. S. Hepburn, K. Jeong, I. L. Chin, R. W. Sanderson, J. H. Jeong, Z. M. Aman, B. F. Kennedy, Y. Hwang, D. W. Han, H. W. Park, K. L. Guan, J. P. Spatz, Y. S. Choi, *ACS Appl. Mater. Interfaces* **2019**, *11*, 45520.
- [33] a) H. P. Lee, L. Gu, D. J. Mooney, M. E. Levenston, O. Chaudhuri, *Nat. Mater.* **2017**, *16*, 1243; b) Z. Gong, S. E. Szczesny, S. R. Caliri, E. E. Charrier, O. Chaudhuri, X. Cao, Y. Lin, R. L. Mauck, P. A. Janmey, J. A. Burdick, V. B. Shenoy, *Proc. Natl. Acad. Sci. USA* **2018**, *115*, E2686.
- [34] P. W. Oakes, T. C. Bidone, Y. Beckham, A. V. Skeeters, G. R. Ramirez-San Juan, S. P. Winter, G. A. Voth, M. L. Gardel, *Proc. Natl. Acad. Sci. USA* **2018**, *115*, 2646.
- [35] S. D. Chandradoss, A. C. Haagsma, Y. K. Lee, J.-H. Hwang, J.-M. Nam, C. Joo, *J. Visualized Exp.* **2014**, *24*, e50549.
- [36] M. T. Yang, N. J. Sniadecki, C. S. Chen, *Adv. Mater.* **2007**, *19*, 3119.
- [37] B. G. Ricart, M. T. Yang, C. A. Hunter, C. S. Chen, D. A. Hammer, *Biophys. J.* **2011**, *101*, 2620.

# ADVANCED BIOSYSTEMS

## Supporting Information

for *Adv. Biosys.*, DOI: 10.1002/adbi.202000012

Hydrogel Micropost Arrays with Single Post Tunability to  
Study Cell Volume and Mechanotransduction

*Daniel Devine, Vishwaarth Vijayakumar, Sing Wan Wong,  
Stephen Lenzini, Peter Newman, and Jae-Won Shin\**



## Supporting Information

**Title:** Hydrogel micropost arrays with single post tunability to study cell volume and mechanotransduction

**Authors:** Daniel Devine<sup>1,2#</sup>, Vishwaarth Vijayakumar<sup>1,2#</sup>, Sing Wan Wong<sup>1,2#</sup>, Stephen Lenzini<sup>1,2</sup>, Peter Newman<sup>1,2+</sup>, Jae-Won Shin<sup>1,2\*</sup>

### Affiliations:

<sup>1</sup>Department of Pharmacology and Regenerative Medicine, University of Illinois at Chicago, Chicago, IL, USA

<sup>2</sup>Department of Bioengineering, University of Illinois at Chicago, Chicago, IL, USA

<sup>#</sup>Equal contribution

<sup>+</sup>Current address: University of Sydney, Sydney, Australia

<sup>\*</sup>Correspondence to J-W. S.: [shinjaw@uic.edu](mailto:shinjaw@uic.edu)

**Keywords:** mechanobiology; extracellular matrix; cell volume; hydrogels; microposts

This file contains:

Supporting Figures 1-6

## Supporting Figures

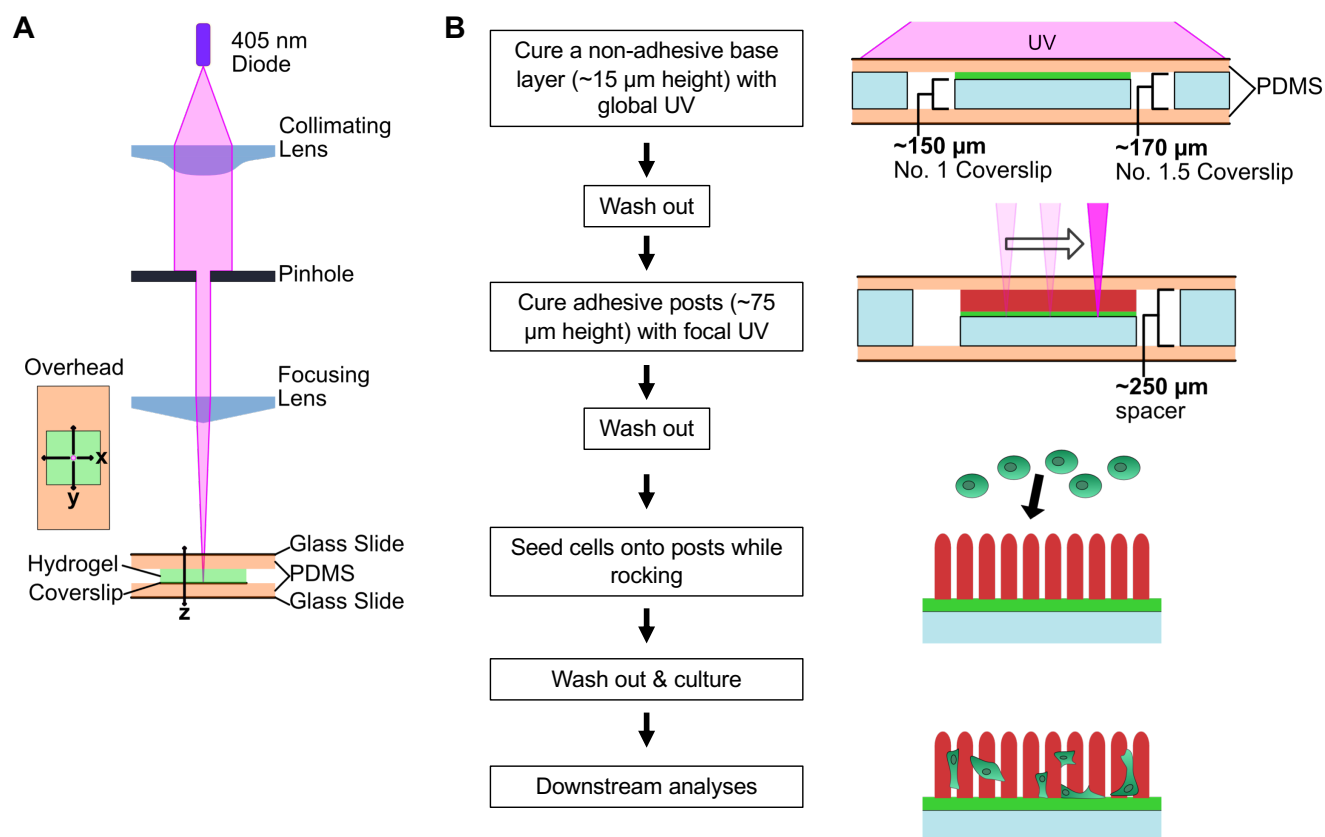


**Figure S1. Freeform stereolithography.** (A) Schematic illustration of custom print head and scaffold printing chamber used to print microposts. (B) General process flow used to print micropost scaffolds and use for biological experiments, with schematic illustration of print chamber during base layer and post fabrication. The base layer was cured by UV lamp exposure for 90 seconds, and washed three times with post hydrogel solution prior to printing microposts with cRGD-containing hydrogel. All hydrogels were washed out for 1-3 days prior to experiments.

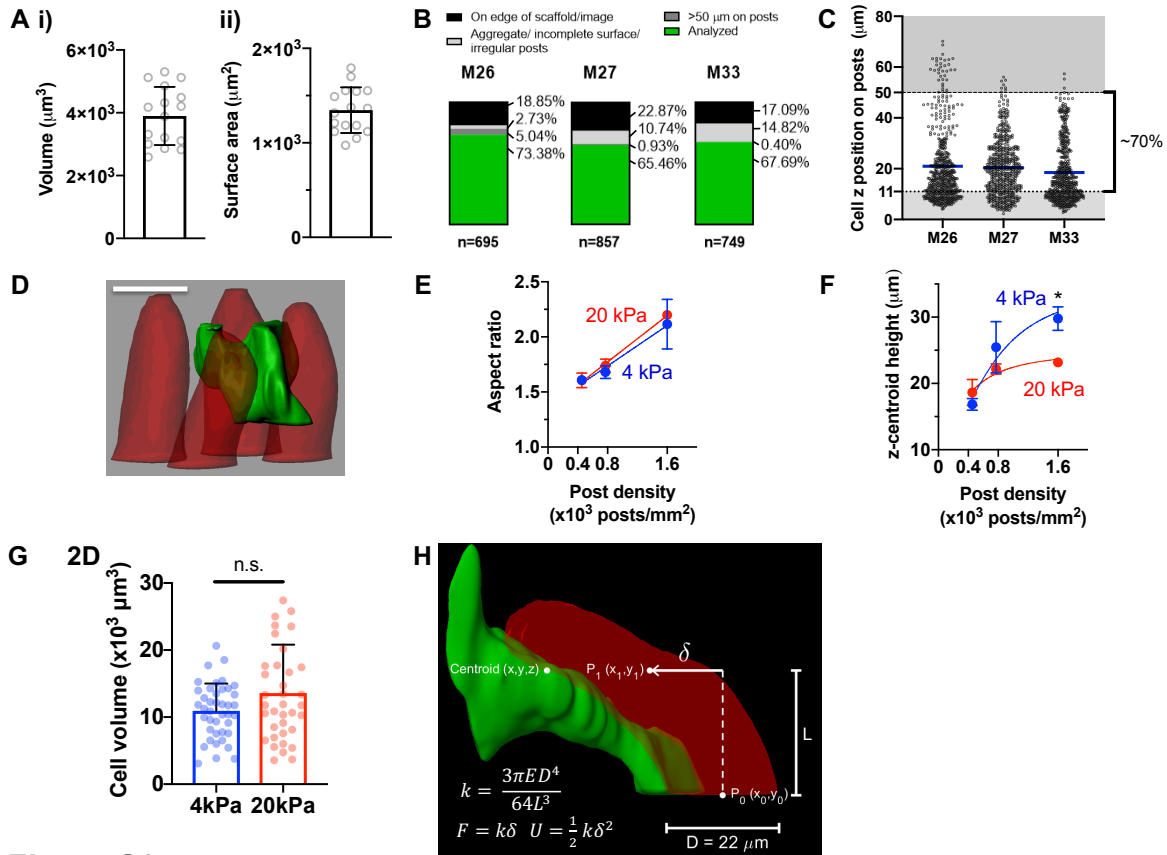


**Figure S2. Characterization of MSCs in hydrogel micropost arrays.** (A) (i) Volume and (ii) surface area of individual MSCs immediately after ( $< 2$  h) embedded in collagen;  $n = 16$ . Error bars: SD. (B) Exclusion analysis of cells from 3 donors. 3D reconstruction of cells from confocal images was done in Imaris based on fluorescence intensity of CellMask Green plasma membrane stain. Cells attached to scaffold boundary or clipped at edge of the confocal image were excluded from analysis. Cells were further excluded due to aggregation (2 or more cells in contact), incomplete membrane stain/surface rendering, primarily contacting irregular posts, or being located outside the linear cell attachment region ( $> 50 \mu\text{m}$  in height from the post base). (C) Distribution of cell positions along the posts after 24h culture. Cell positions are defined as the centroid z coordinate (mean vertical position) relative to post base positions. 2.9% of all cells were located outside the linear cell attachment region of the post, while  $\sim 70\%$  of all cells were located between 11-50  $\mu\text{m}$ ;  $n \geq 695$  per donor. (D) Representative images showing a live MSC located in the interstitial spaces between microposts above a base layer. Scale bar = 25  $\mu\text{m}$ . (E) Aspect ratio of MSCs. Points were fit to linear regression,  $Y = Y_0 + AX$ . ( $Y_0$ ,  $A$ ) values for 4 kPa = (1.37, 459.4), for 20 kPa = (1.35, 525.9). (F) Average centroid z height of MSCs. Dose response fit (Fig. 2) values (min, max, potency, b) for 4 kPa = (11, 35, 729, 1.96), for 20 kPa = (11, 25, 387, 1.56). For (E) and (F), data points were plotted as a function of post density in 4-kPa or 20-kPa arrays.  $*p < 0.05$ , two-way repeated measures ANOVA followed by Tukey's multiple comparisons test. Error bars represent the SEM of the mean values across 3 different MSC donors.  $n \geq 70$  cells per donor. (G) Cell volume on 2D PEG-DA gels with cRGD. Error bars: SD;  $n \geq 37$  cells pooled from 3 independent experiments. (H) Illustration of the approach used to calculate the Hookean force and strain energy that cells applied to bend posts.  $k$ , the spring constant, was defined in terms of  $E$ , the elastic modulus of the post (4 or 20 kPa);  $D$ , the diameter of the post; and  $L$ , the height of the centroid of the cell from the base of the post in the  $z$  direction.  $\delta$ , the deflection of the post, was measured between the centroid of the base of the post ( $P_0$ ) and the centroid of the post at the  $z$ -stack image corresponding to the height of the centroid of the cell ( $P_1$ ).

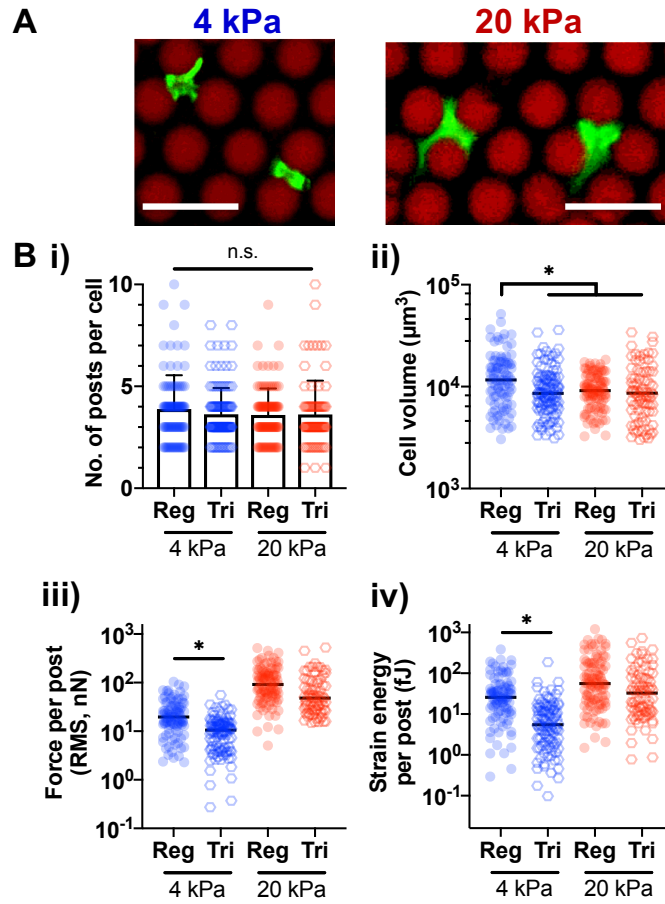


**Figure S3. Characterization of cell volume, traction force and strain energy in arrays with triangular post arrangement.** (A) Representative image showing live MSCs seeded in triangular micropost arrays. Scale bar = 50  $\mu\text{m}$ . (B) Quantification of (i) number of posts per cell, (ii) cell volume, (iii) average force per post, (iv) strain energy per post. Reg: regular array, Tri: triangular array.  $*p < 0.05$ , Kruskal-Wallis test, followed by Dunn's multiple comparisons test. Error bars in (i) represent SD, and median values are shown in (ii)-(iv);  $n \geq 85$  for each group pooled from 3 independent experiments, 1 donor.

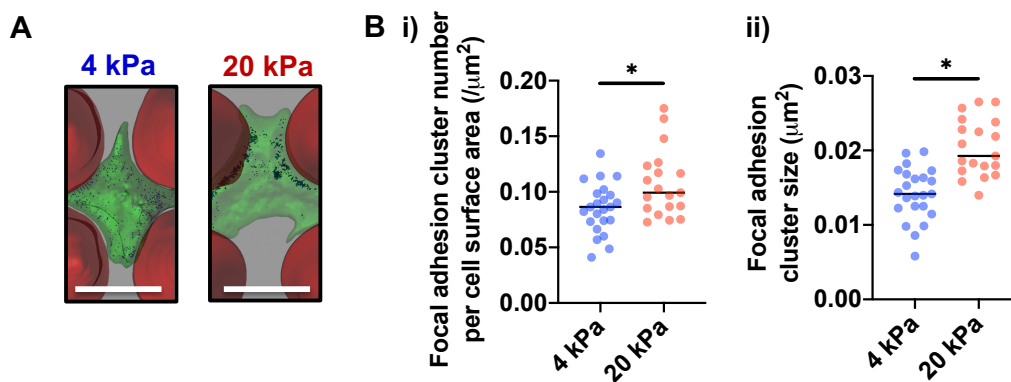


**Figure S4. Quantification of paxillin<sup>+</sup> focal adhesion in MSCs adhered to micropost arrays. (A)** Representative images showing live MSCs (transparent green, labelled with plasma membrane stain) that express paxillin-RFP puncta (dark green) in micropost arrays (red). Scale bar = 20  $\mu\text{m}$ . **(B)** Quantification of paxillin-RFP puncta in terms of (i) cluster number per cell surface area, and (ii) average cluster size per cell.  $*p < 0.05$ , two-tailed Welch's T-test. Median values are shown for each group;  $n \geq 20$  cells for each group pooled from 3 independent experiments, 1 donor.



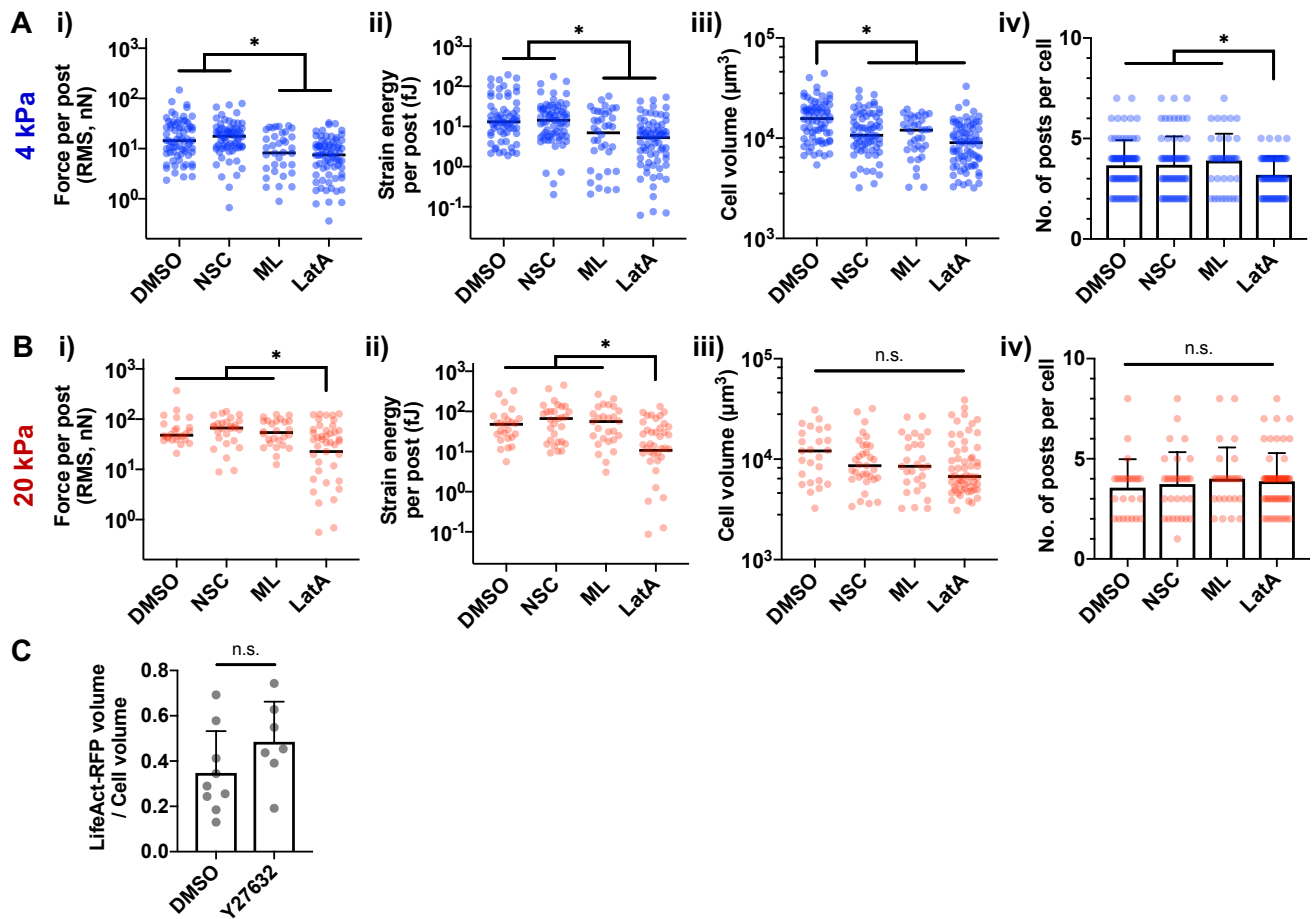


**Figure S5. Effects of Rac, Cdc42 and actin polymerization on MSCs in micropost arrays.** MSCs in micropost arrays were treated with DMSO, the Rac inhibitor NSC23766 (“NSC”, 10  $\mu\text{M}$ ), the Cdc42 inhibitor ML141 (“ML”, 10  $\mu\text{M}$ ) or latrunculin A (“LatA”, 0.25  $\mu\text{M}$ ) for 4 hours prior to analysis. Effects of inhibitors on MSCs in (A) 4-kPa arrays and (B) 20-kPa arrays. For (A) and (B), (i) average force per post, (ii) average strain energy per post, (iii) cell volume, (iv) number of interacting posts per cell. \* $p < 0.05$ , Kruskal-Wallis test, followed by Dunn’s multiple comparisons test. For (i)-(iii), median values are shown, and error bars in (iv) represent SD.  $n \geq 25$  for each group pooled from 2 independent experiments, 1 donor. (C) Quantification of F-actin in live MSCs. After transfection with LifeAct-RFP, MSCs were seeded in 4-kPa arrays for 24 hours, followed by treatment with DMSO or Y27632 for 24 hours;  $n \geq 7$  cells for each group.

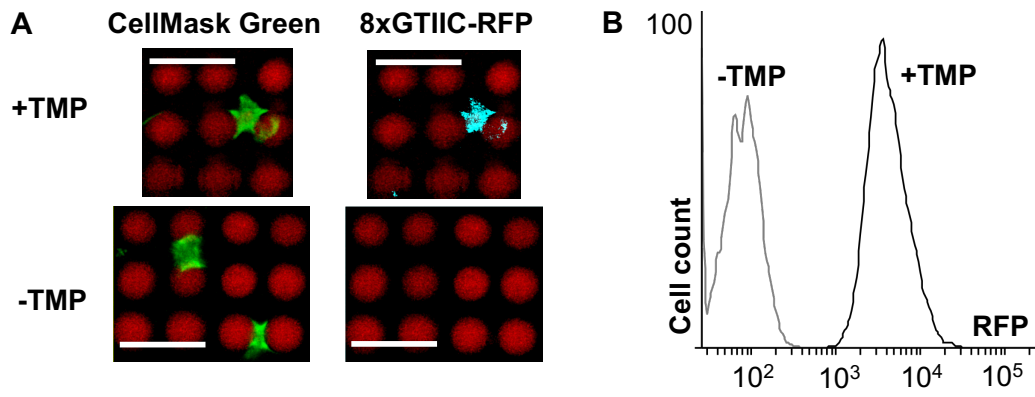


**Figure S6. YAP-responsive reporter expression.** (A) Representative images showing YAP reporter transfected MSCs in 20-kPa posts. CellMask Green: plasma membrane, 8xGTIIC-RFP: RFP reporter expressed as a function of YAP activity on the 8XGTIIC promoter. RFP is fused with a destabilization domain (DD) that is stabilized only in the presence of trimethoprim (TMP). Thus, RFP signals are not detectable above the background level in the absence of TMP. Scale bar = 50  $\mu$ m. (B) Representative flow cytometry histogram showing cell population of YAP reporter transfected MSCs with or without TMP.